

Resolution Limits of Resonant Sensors

Manzaneque, Tomás; Ghatkesar, Murali K.; Alijani, Farbod; Xu, Minxing; Norte, Richard A.; Steeneken, Peter G.

DOI

[10.1103/PhysRevApplied.19.054074](https://doi.org/10.1103/PhysRevApplied.19.054074)

Publication date

2023

Document Version

Final published version

Published in

Physical Review Applied

Citation (APA)

Manzaneque, T., Ghatkesar, M. K., Alijani, F., Xu, M., Norte, R. A., & Steeneken, P. G. (2023). Resolution Limits of Resonant Sensors. *Physical Review Applied*, 19(5), Article 054074. <https://doi.org/10.1103/PhysRevApplied.19.054074>

Important note

To cite this publication, please use the final published version (if applicable). Please check the document version above.

Copyright

Other than for strictly personal use, it is not permitted to download, forward or distribute the text or part of it, without the consent of the author(s) and/or copyright holder(s), unless the work is under an open content license such as Creative Commons.

Takedown policy

Please contact us and provide details if you believe this document breaches copyrights. We will remove access to the work immediately and investigate your claim.


Resolution Limits of Resonant Sensors

Tomás Manzaneque^{1,*}, Murali K. Ghatkesar², Farbod Alijani², Minxing Xu^{2,3}, Richard A. Norte^{2,3}
and Peter G. Steeneken^{2,3}

¹*Department of Microelectronics, Delft University of Technology, Netherlands*

²*Department of Precision and Microsystems Engineering, Delft University of Technology, Netherlands*

³*Department of Quantum Nanoscience, Delft University of Tehcnology, Netherlands*

 (Received 11 November 2022; revised 3 April 2023; accepted 21 April 2023; published 23 May 2023)

Resonant sensors hold great promise in measuring small masses, to enable future mass spectrometers, and small forces in applications like atomic and magnetic force microscopy. During the last decades, scaling down the size of resonators has led to huge enhancements in sensing resolution, but has also raised the question of what the ultimate limit is. Current knowledge suggests that this limit is reached when a resonator oscillates at the maximum amplitude for which its response is predominantly linear. We present experimental evidence that it is possible to obtain better resolutions by oscillation amplitudes beyond the onset of nonlinearities. An analytical model is developed that explains the observations and unravels the relation between ultimate sensing resolution and speed. In the high-speed limit, we find that the ultimate resolution of a resonator is improved when decreasing its damping. This conclusion contrasts with previous works, which proposed that lowering the damping does not affect or even harms the ultimate sensing resolution.

DOI: [10.1103/PhysRevApplied.19.054074](https://doi.org/10.1103/PhysRevApplied.19.054074)

I. INTRODUCTION

The use of mechanical resonators as precise sensors for mass, force, and other physical parameters has been fueled by recent advances in miniaturization. This is because a lower resonator mass leads to a higher responsivity, i.e., a larger shift of the resonance frequency for a given stimulus [1]. However, the detection limit of resonant sensors is not only determined by the responsivity, but also by the frequency resolution, which is defined as the smallest resonance frequency change that can be detected. In order to be resolved, a frequency change needs to be larger than the stochastic variations observed when measuring the resonance frequency, which are commonly characterized by the Allan deviation σ_y [2,3]. The Allan deviation of a resonant sensor results from the noise sources inherent to the resonator, its environmental conditions, and the noise from the readout [1,4–6]. When all environmental and readout noise sources are eliminated, the fundamental resolution limit at finite temperatures is determined by the resonator's thermomechanical noise. The corresponding Allan deviation, which depends on the integration time of the measurement, has been well established for mechanical resonators in the linear regime [1,7].

The linear harmonic oscillator model does not predict a lower limit for the Allan deviation, since increasing the

actuation power, and so the signal-to-noise ratio, always results in a lower Allan deviation σ_y for a given integration time. Several authors have pointed out that this trend cannot continue indefinitely for real resonators, due to the appearance of nonlinear effects at high enough actuation powers [1,7–10]. For mechanical resonators at the micro- and nanoscale, nonlinear effects usually manifest as a cubic stiffness in the resonator dynamics, commonly known as Duffing nonlinearity. This characteristic comes with conversion of amplitude noise into phase noise that enhances with the actuation power, worsening the frequency resolution. Therefore, it is expected that Duffing resonators present an optimum power level as a result of the trade-off between signal-to-noise ratio and amplitude-phase noise conversion. Following this rationale, it has been assumed that the minimum Allan deviation is obtained for a characteristic oscillation amplitude at which the nonlinear effects become dominant, known as the critical amplitude or onset of nonlinearity [7–9]. Using the fact that this critical amplitude is inversely proportional to the quality factor Q , it has been proposed that the minimum Allan deviation is independent of Q [7,9]; see Fig. 1. Using the same argument, Roy *et al.* [8] concluded that the minimum Allan deviation can be even reduced by decreasing the quality factor of a resonator; see Fig. 1(a). Differently from previous studies, this study did not include the dynamics of the closed-loop controller often used to drive resonant sensors [7]. With or without the closed-loop dynamics, the results

*t.manzanequegarcia@tudelft.nl

cited noticeably contrast with historical efforts of the resonant sensor community to increase the quality factor of mechanical resonators to improve resolution.

Besides resolution, fast reading is an important requisite in most applications of resonant sensors. For example, the scan speed in atomic force microscopy is key to characterize dynamic biomolecular processes [11]. The analysis of the proteom of single cells has been envisioned with nanomechanical resonators [12], for which millions of molecules need to be individually weighted. Nevertheless, for a linear resonator at a given oscillation amplitude, the resolution scales with inverse proportionality to the integration time [4], such that faster measurements result in worse resolution (higher Allan deviation). This reduction in precision can be compensated by increasing the oscillation amplitude, but only within the linear range. Therefore, using the critical amplitude argument described above, previous knowledge suggests that nonlinearities fundamentally limit the sensing speed for a given resolution level.

In this work, we experimentally and theoretically analyze the ultimate frequency resolution of Duffing resonators under closed-loop operation. Our experimental results show that sensor resolution can be improved beyond the previously determined limits [7,9] for integration times τ shorter than a critical time constant of

approximately Q/f_0 , where Q is the quality factor and f_0 is the linear resonance frequency. To gain insight into the problem, the effect of white noise on the Allan deviation of a Duffing resonator under closed-loop operation is modeled using perturbation theory. The developed model, based on linearization of the amplitude-phase space of the Duffing resonator, closely reproduces our experimental findings. In addition, the theory provides useful expressions to determine the lower limit for the Allan deviation in the nonlinear regime, and the optimal actuation level needed to reach it, which turns out to depend on the integration time.

Our results show that two regimes can be identified in which the minimum Allan deviation of a Duffing resonator, which defines its ultimate resolution limit, exhibits distinct behaviors. For fast sensing (short integration times), the ultimate resolution limit is independent of the integration time, which implies that it can be attained at arbitrarily high speeds. Furthermore, this limit can be improved by increasing the resonator's quality factor. For slow sensing (long integration times), the ultimate resolution limit does not depend on the quality factor as long as all other resonator characteristics are left unchanged. Figure 1(c) shows a graphical representation of the determined resolution limits and their dependence on the quality factor and the integration time.

In the following, we first present an experimental study of the frequency resolution of a nonlinear silicon nitride nanomechanical membrane and its dependence on driving power and the integration time. Then we theoretically analyze the resolution limits of Duffing resonators and derive analytic expressions for the minimum Allan deviation, for limiting cases of short and long integration times. Finally, we perform numerical simulations of the Duffing resonator under closed-loop operation to validate the analytical model, and confirm the conclusions without the linearization approximations introduced in the analytical derivations.

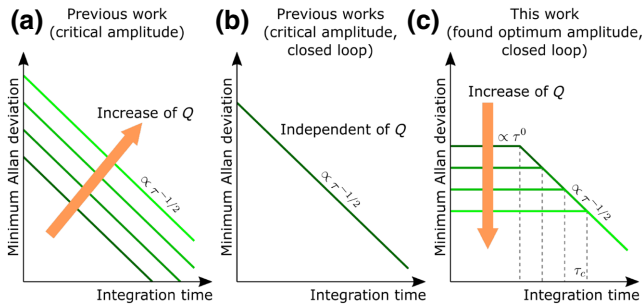


FIG. 1. Log-log plots of the minimum Allan deviation that can be obtained by a thermomechanically limited Duffing resonator when optimizing the actuation power, as a function of the integration time τ . Each curve within the same plot corresponds to a different value of the quality factor. (a) Limit found by Roy *et al.* [8] by assuming that the minimum Allan deviation is reached for actuation at the critical amplitude. (b) Limit found by Olcum *et al.* [9] for high quality factor resonators, and by Demir and Hanay [7] for any quality factor but assuming a closed-loop operation. Both works use the assumption that the minimum Allan deviation is reached at or close to the critical amplitude. (c) Limit for Duffing resonators under closed-loop operation, by using the optimum actuation amplitude found in this work, that depends on the integration time. For short integration times, the minimum Allan deviation is independent of the integration time. For long integration times, the minimum Allan deviation shows a $\tau^{-1/2}$ dependence and matches the result in (b). The transition between both regimes occurs at $\tau_c = \sqrt{3}Q/(\pi f_0)$.

II. EXPERIMENTAL RESULTS

A series of experiments is performed on a square silicon nitride membrane with a thickness of 92 nm and an area of $2 \times 2 \text{ mm}^2$ that is suspended on a silicon chip; see Figs. 2(a) and 2(b). The chip is mounted on a piezoactuator inside a vacuum chamber at a pressure of 2 mPa (see Appendix A). The motion in the center of the membrane is recorded by Doppler laser vibrometry. The measurement setup is sensitive enough to characterize the resonator's thermomechanical displacement noise in the absence of piezoactuation, whose power spectral density (PSD) spectrum is shown in Fig. 2(c). The figure shows a peak at 188 kHz that corresponds to the fundamental vibration mode of the membrane. The peak has an amplitude 6.3 times larger than the measurement noise floor allowed

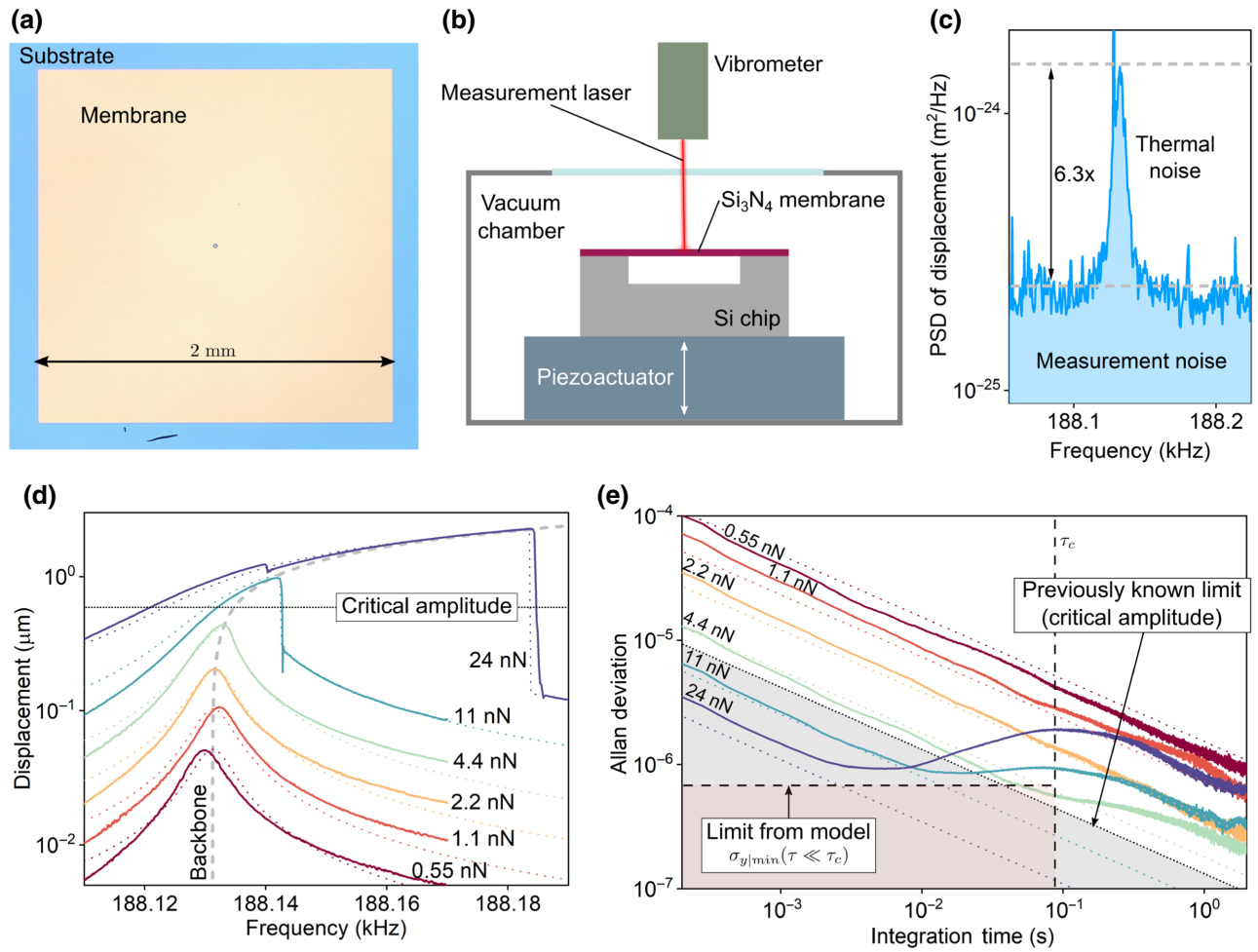


FIG. 2. (a) Top-view optical picture of the Si_3N_4 membrane used in the experiments. (b) Cross-section representation of the chip containing the membrane in the experimental setup. (c) Measured noise spectrum in the absence of actuation. The peak corresponds to the thermomechanical noise of the membrane's fundamental resonance. (d) The solid lines represent experimental upward frequency sweeps around the fundamental resonance for different actuation levels. For low levels, the membrane behaves as a linear resonator. For 4.4 nN and above, a stiffening effect is observed that produces bifurcation for 11 nN and above. The dotted lines represent fittings to the Duffing model for each actuation level, using the values in Table I. The backbone curve described by Eq. (1) is plotted for reference. The critical amplitude calculated from γ and Q [13], $a_{\text{crit}} = 0.59 \mu\text{m}$, is also indicated. (e) Dimensionless Allan deviation for the same actuation levels as in (d), when the membrane is driven by a PLL controller at the displacement maxima. The solid lines represent measurements, where white force noise with PSD $S_0 = 2.5 \times 10^{-21} \text{ N}^2 \text{ Hz}^{-1}$ is added to the actuation to ensure that the response is dominated by white force noise. This force noise resembles the thermomechanical noise the resonator would experience at temperatures higher than room temperature. The dotted colored lines represent the theoretical values for the membrane assuming a linear response under the experimental conditions. The dotted black line indicates the previously known limit for the Allan deviation, defined by actuation at the critical amplitude. The horizontal dashed line indicates the lower boundary for the Allan deviation found by our model at integration times below τ_c .

to extract the linewidth. The modal stiffness defining the linear resonance, specified in Table I, is obtained by fitting the PSD data using the equipartition theorem [14]. Then, upward frequency sweeps are performed around the found resonance with different actuation levels, with the results plotted in Fig. 2(d). The experimental curves are fitted to a Duffing model to obtain the rest of the parameters defining

the resonance, listed in Table I, as well as the applied force values. As the actuation level increases, a hardening effect becomes evident from the bending of the resonance peak to the right. For an actuation force of 11 nN and above, a sudden jump in the displacement amplitude is observed, which indicates that the critical amplitude has been surpassed, i.e., the resonator shows bifurcation [13]. For 24 nN, a dip

TABLE I. Resonator parameters obtained from the experiments. The modal stiffness is obtained by fitting the data in Fig. 2(c) using the equipartition theorem. Then, the resonance frequency, modal mass, quality factor, and Duffing parameter are obtained by fitting the curves in Fig. 2(d) to the Duffing model.

Resonance frequency	Quality factor	Modal stiffness	Modal mass	Duffing coefficient
f_0	Q	k_1	m	γ
188.1 kHz	30×10^3	320 N m^{-1}	229 ng	$1.47 \times 10^8 \text{ m}^{-2}$

is seen in the response curve at 188.14 kHz, which suggests nonlinear coupling with a higher order mode [15]. The displacement maxima, with amplitude a_p for each actuation level, follow the backbone curve of Duffing resonators [16],

$$\omega_p = \omega_0 \left(1 + \frac{3}{8} \gamma a_p^2 \right) \quad (1)$$

with ω_p the angular frequency at which amplitude a_p is reached and ω_0 the angular resonance frequency in the linear regime. Parameter γ is the Duffing coefficient, defined as the cubic stiffness divided by the linear stiffness; see Eq. (5) below. The characteristic backbone curve of our resonator model is plotted in Fig. 2(d).

Next, to evaluate the effects of thermomechanical noise on the Allan deviation of the closed-loop-driven Duffing resonator, experiments in the presence of white force noise are performed. For that, a phase locked-loop (PLL) control scheme is set to continuously drive the resonator at resonance (see Appendix A), with PLL parameters set using the method described in Ref. [17]. The chosen configuration ensures that the observed Allan deviation is independent of the PLL parameters for integration times longer than 100 μs . The controller is set to target a phase shift of $-\pi/2$ in the resonator's response, where phase shifts introduced by other components are compensated for. This condition ensures that the device is driven at ω_0 when the applied force is in the linear regime, and at the nonlinear resonance frequency ω_p when the resonator enters the nonlinear regime [18]. Note that the nonlinear coupling seen for 24 nN occurs at frequencies far from ω_p ; therefore, it is not expected to affect the Allan deviation measurements.

The experimental analysis of resonators at their thermomechanical limits is hindered by resonance frequency fluctuations [5] and the presence of measurement noise introduced by instrumentation. To illustrate the challenge to study the Allan deviation of micro- and nanomechanical resonators in the absence of measurement noise, we note that to reach that condition the thermomechanical noise peak in Fig. 2(c) would have to exceed the background PSD at $f < f_0$ by a factor $4Q^2 \Delta f^2 / f_n^2$ [19], where Δf is the measurement bandwidth that limits the minimum integration time for which the Allan deviation can

be determined. For our device, this translates into a factor of 1×10^7 , which is much higher than the experimental ratio of 6.3. To overcome this problem, we ensure that the resonator operates in the regime where its response is dominated by white force noise by using the piezo to add a random force, with white spectral distribution and PSD S_0 , to the sinusoidal actuation force provided by the PLL system. According to the fluctuation-dissipation theorem, the thermomechanical noise of a system is fully accounted for by a force of such type and power spectral density (one sided, on a per hertz basis) [20]

$$S_{\text{thm}} = 4ck_B T, \quad (2)$$

where k_B is the Boltzmann constant, T is the absolute temperature, and c is the dissipation constant of the system. For either linear or Duffing resonators, $c = \sqrt{k_1 m / Q}$, where k_1 is the linear modal stiffness, m is the modal mass, and Q is the quality factor. By adding white noise with PSD S_0 , we emulate the thermomechanical noise the resonator would experience at a higher effective temperature $T_{\text{eff}} = S_0 / (4ck_B)$. Making S_0 much larger than the other noise sources ensures that the Allan deviation is limited by this artificial thermomechanical noise. Thus, our experiments capture the ultimate situation where thermomechanical noise dominates the frequency resolution, such that contributions of instrumentation and fluctuations on the operation conditions can be neglected. In all of the Allan deviation experiments, the amplitude of the white noise is set to a constant value of $S_0 = 2.5 \times 10^{-21} \text{ N}^2 \text{ Hz}^{-1}$.

In Fig. 2(e) (solid lines), we report the dimensionless Allan deviations measured at the same actuation forces as in Fig. 2(d). The diagonal dotted lines represent the calculated Allan deviation for linear resonators under closed-loop operation [7]:

$$\sigma_{y,0}(\tau) = \frac{1}{a_x} \sqrt{\frac{k_B T}{m Q \omega_0^3 \tau}} \quad (3)$$

with τ the integration time and a_x the displacement amplitude of the oscillation. Note that the phase condition $\phi = -\pi/2$ set in the experiments ensures that the driving frequency equals ω_p and therefore a_x equals the peak amplitude a_p . It is observed that, for force amplitudes in the linear range of operation (0.55, 1.1, and 2.2 nN), the measured Allan deviation shows good agreement with Eq. (3).

At actuation force levels of 4.4 nN and above, where the resonator response in Fig. 2(d) is seen to enter the non-linear regime, the measured Allan deviation in Fig. 2(e) is seen to differ strongly in behavior from the linear model, with three distinguishable regimes. In the first regime, for short integration times τ , the Allan deviation behaves as predicted by the linear model, with a $\tau^{-1/2}$ dependence like in Eq. (3) (indicated by dotted lines in the figure). Note that the Allan deviation is not affected by the Duffing nonlinearity in this regime, even for actuation forces that exceed the critical amplitude (11 and 24 nN). At intermediate values of τ , the Allan deviation increases significantly. Finally, in the third regime at integration times longer than approximately Q/f_0 , the Allan deviation reduces again with a $\tau^{-1/2}$ trend, although at significantly higher levels than obtained from Eq. (3). In this last regime, the data correspond well to the theoretical prediction from Ref. [7], with the lowest Allan deviation being found at a driving force of 4.4 nN, which is the force that is closest to the critical amplitude in Fig. 2(d). However, this driving force does not give the lowest Allan deviation for all integration times, since the curves at 11 and 24 nN show lower values in the region $\tau < Q/f_0$. In addition, these curves show local minima at an approximately constant value of the Allan deviation. In the next sections, this behavior of the Allan deviation in the nonlinear regime is analyzed further by theory and simulations.

III. THEORY AND MODEL

For a driven Duffing resonator, the modal displacement x and modal force g are related by the second-order differential equation

$$m\ddot{x}(t) + c\dot{x}(t) + k_1x(t) + k_3x^3(t) = g(t), \quad (4)$$

where t represents the time and k_3 is the cubic stiffness of the vibration mode. This equation can be simplified by normalizing the time, $\hat{t} = t\omega_0$, and the force, $\hat{g} = g/k_1$, resulting in

$$\ddot{x}(\hat{t}) + 2\Gamma\dot{x}(\hat{t}) + x(\hat{t}) + \gamma x^3(\hat{t}) = \hat{g}(\hat{t}), \quad (5)$$

where $\Gamma = 1/(2Q)$ is the damping ratio and $\gamma = k_3/k_1$ is the Duffing coefficient.

Let the displacement and force be approximately harmonic functions of \hat{t} , $x(\hat{t}) = a_x(\hat{t}) \sin(\hat{\omega}\hat{t} + \phi_x(\hat{t}))$ and $\hat{g}(\hat{t}) = a_g(\hat{t}) \sin(\hat{\omega}\hat{t} + \phi_g(\hat{t}))$, respectively, with $\hat{\omega} = \omega/\omega_0$. The amplitudes and phases are assumed to vary slowly, at characteristic times much longer than the inverse of the resonance frequency ω_0 . In the high- Q limit, the slow dynamics of the resonator can be modeled by

applying the method of averaging [16,21]:

$$\dot{a}_x = -\Gamma a_x - \frac{1}{2}a_g \sin \phi \equiv \eta_a, \quad (6)$$

$$\dot{\phi}_x = \frac{3}{8}\gamma a_x^2 - \psi - \frac{1}{2}\frac{a_g}{a_x} \cos \phi \equiv \eta_\phi, \quad (7)$$

$$\dot{\phi} = \phi_x - \phi_g. \quad (8)$$

Here $\psi = \hat{\omega} - 1$ is the detuning of the normalized actuation frequency, where $\psi = 0$ represents the tuned condition in which the resonator is actuated at ω_0 .

Equations (6)–(8) describe a system of nonlinear differential equations that relate the amplitude and phase of the displacement to the amplitude and phase of the applied force. As detailed in Appendix B, this system can be linearized around a fixed point and translated into the Laplace domain to obtain a matrix of transfer functions $H(s)$ that relates the inputs to the outputs:

$$\begin{bmatrix} A_x(s) \\ \Phi_x(s) \end{bmatrix} = \begin{bmatrix} H_{11}(s) & H_{12}(s) \\ H_{21}(s) & H_{22}(s) \end{bmatrix} \begin{bmatrix} A_g(s) \\ \Phi_g(s) \end{bmatrix}. \quad (9)$$

Here A_x , Φ_x , A_g , and Φ_g represent the Laplace transforms of the small perturbations of a_x , ϕ_x , a_g , and ϕ_g , respectively, around the fixed point, while s denotes the Laplace variable. Matrix $H(s)$ depends on Γ , γ , and the chosen fixed point.

A closed-loop driving scheme is necessary in most practical sensors operating in the linear regime to keep the resonator's phase shift ϕ close to $-\pi/2$ upon significant shifts of the resonance frequency. Additionally, in the nonlinear regime a closed-loop scheme allows for controlling the amplitude of vibration and therefore the fixed point of operation. This is done by fixing either a_x or a_g . The variables that define the fixed point, at which $\dot{a}_x = 0$ and $\dot{\phi}_x = 0$, are found from Eqs. (6)–(8) to be related through

$$a_g = -\frac{2\Gamma a_x}{\sin \phi}, \quad (10)$$

$$\psi = \frac{3}{8}\gamma a_x^2 + \frac{\Gamma}{\tan \phi}. \quad (11)$$

For a given fixed point, a resonator driven by a closed-loop system will operate at a constant detuning given by Eq. (11). Therefore, the drive frequency ω keeps a constant relation with ω_0 , such that an estimator for the resonance frequency can be defined as

$$\bar{\omega}_0 = \frac{\omega}{1 + 3\gamma a_x^2/8 + \Gamma/\tan \phi}. \quad (12)$$

For a linear resonator driven at $\phi = -\pi/2$, ω is directly the estimator for ω_0 and presents no bias. The bias of the estimator for a nonlinear resonator is discussed in Appendix C.

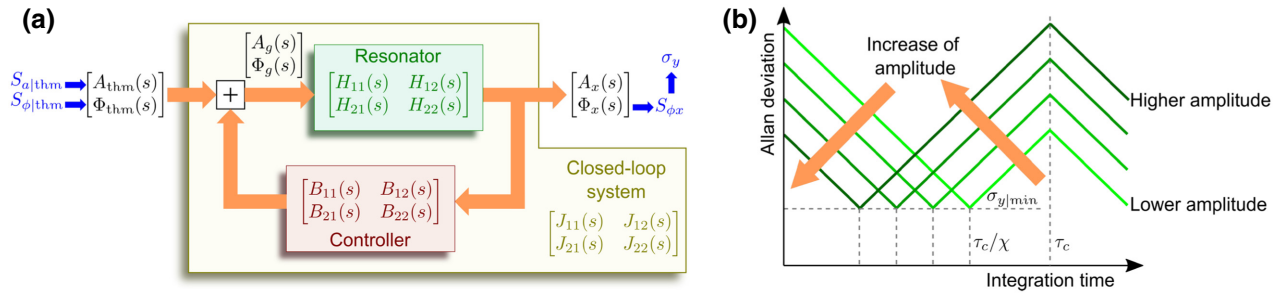


FIG. 3. (a) Laplace-domain block diagram of the linearized small-signal model of the resonator and the resonance-tracking control loop. The closed-loop system matrix $J(s)$ governs the conversion of amplitude and phase perturbations at the input (force) into amplitude and phase perturbations at the output (displacement). We highlight blue the input and output magnitudes used in the analysis. Amplitude and phase random perturbations due to thermomechanical noise, with PSDs $S_{a|\text{thm}}$ and $S_{\phi|\text{thm}}$, respectively, translate into phase perturbations at the output with PSD S_{ϕ_x} , from which the Allan deviation (σ_y) is calculated. (b) Log-log plot of the Allan deviation predicted by the model in (a) for a Duffing resonator at its thermomechanical limit oscillating at $\phi = -\pi/2$. Each curve represents a different amplitude of oscillation. A characteristic minimum $\sigma_{y|\text{min}}$ is reached at an integration time τ_c/χ that depends on the amplitude of oscillation. For $\tau \ll \tau_c/\chi$, the Allan deviation is governed by the linear response and the Duffing term can be neglected ($\gamma = 0$).

It is worth noting that, while the estimator for the linear resonance frequency defined by Eq. (12) is obtained by straightforward generalization from the standard estimator for a closed-loop linear resonator, it might not be optimal for nonlinear resonators. A better estimator could possibly be obtained by Cramer-Rao lower bound analysis [22], but this is beyond the scope of this work. In addition to defining the fixed point of the resonator model, the control loop influences the time evolution of the noise-induced amplitude and phase perturbations around the fixed point. Figure 3(a) shows a block diagram in the Laplace domain of the closed-loop model for the perturbations. A closed-loop transfer function matrix $J(s)$ is defined from the resonator's open-loop transfer function matrix $H(s)$ and the transfer function matrix $B(s)$ of the feedback controller. The derivations of these matrices, which can be found in Appendix B, result in

$$J_{11}(s) = -\frac{\sin \phi}{2(s + \Gamma)}, \quad (13)$$

$$J_{12}(s) = -\frac{\Gamma a_x}{\tan \phi (s + \Gamma)}, \quad (14)$$

$$J_{21}(s) = -\frac{3\gamma a_x^2 \sin \phi + 4s \cos \phi}{8a_x s (s + \Gamma)}, \quad (15)$$

$$J_{22}(s) = \frac{\Gamma(4s \tan^2 \phi - 3\gamma a_x^2 \tan \phi + 4\Gamma(1 + \tan^2 \phi))}{4s(s + \Gamma) \tan^2 \phi}. \quad (16)$$

These equations define a linear model for the amplitude and phase perturbations associated with a Duffing resonator under closed-loop operation. Since this study focuses on the thermomechanical limits, we need to calculate the model inputs that account for thermomechanical noise. In the limit $k_B T \gg \hbar \omega_0$, where \hbar is the reduced

Planck constant, this is achieved by considering a random force with the PSD specified by Eq. (2). When this random force is superimposed on a harmonic actuation force, the result is a quasiharmonic total force with amplitude and phase random perturbations. We can obtain the PSD of the force phase perturbations $S_{\phi|\text{thm}}$ as the PSD of the thermomechanical force divided by the mean value of the force carrier squared [23], $a_g^2 k_1^2 / 2$. Using Eq. (10), we obtain

$$S_{\phi|\text{thm}} = \frac{2S_{\text{thm}}}{a_g^2 k_1^2} = \frac{8k_B T Q \sin^2 \phi}{m \omega_0^3 a_x^2}. \quad (17)$$

Since thermomechanical noise is additive and uncorrelated with the force carrier, the PSD of the normalized amplitude perturbations will be the same as for the phase perturbations [23]. The non-normalized version to be used as input in our model results from multiplying $S_{\phi|\text{thm}}$ by the carrier amplitude squared, a_g^2 , which gives

$$S_{a|\text{thm}} = \frac{2S_{\text{thm}}}{k_1^2} = \frac{8k_B T}{Q m \omega_0^3}. \quad (18)$$

With the PSD of the inputs, we can calculate the PSD of the output amplitude and phase perturbations, S_{ax} and S_{ϕ_x} , respectively, through the relation

$$\begin{bmatrix} S_{ax}(\omega) \\ S_{\phi_x}(\omega) \end{bmatrix} = \begin{bmatrix} |J_{11}(i\hat{\omega})|^2 & |J_{12}(i\hat{\omega})|^2 \\ |J_{21}(i\hat{\omega})|^2 & |J_{22}(i\hat{\omega})|^2 \end{bmatrix} \begin{bmatrix} S_{a|\text{thm}} \\ S_{\phi|\text{thm}} \end{bmatrix}, \quad (19)$$

where i is the imaginary unit. With the last equation, the amplitude and phase noise of the resonator's displacement in a closed-loop configuration can be obtained. The latter is the relevant quantity for the present study as it determines the Allan deviation of the displacement signal, which is a measure of the minimum resonance frequency shift that

can be resolved from the resonator under closed-loop operation. With this model, an analysis of the displacement phase noise S_{ϕ_x} as a function of the phase shift ϕ and the displacement amplitude a_x is given in Appendix D. The results indicate that the Allan deviation of a Duffing resonator can be approximated by three asymptotes at different integration time ranges:

$$\sigma_y(\tau \ll \tau_c/\chi) = \sigma_{y0}, \quad (20)$$

$$\sigma_y(\tau_c/\chi \ll \tau \ll \tau_c) = \sigma_{y0}\chi \frac{\pi}{\sqrt{3}} \frac{f_0\tau}{Q}, \quad (21)$$

$$\sigma_y(\tau \gg \tau_c) = \sigma_{y0}\chi. \quad (22)$$

Each asymptote is expressed as a function of the Allan deviation for linear resonators actuated at resonance σ_{y0} [Eq. (3)] and a factor χ that accounts for the amplitude-phase noise conversion. Defining the normalized amplitude $\hat{a} = a_x/a_{\text{crit}}$, where $a_{\text{crit}} = \sqrt[4]{64/27}/\sqrt{Q\gamma}$ is the critical amplitude [13], this factor can be expressed as

$$\chi = \sqrt{\frac{16}{3}\hat{a}^4 - \frac{8}{\sqrt{3}\tan\phi}\hat{a}^2 + \frac{1}{\sin^2\phi}}. \quad (23)$$

The integration time that defines the boundaries between the different τ ranges is

$$\tau_c = \frac{\sqrt{3}Q}{\pi f_0}. \quad (24)$$

An important observation from this analysis is that the Allan deviation for $\tau \ll \tau_c/\chi$ depends only on the displacement amplitude a_x and not on the particular choice of ϕ and a_g to achieve that value of a_x . This implies that, if the analysis is performed at fixed force amplitude a_g , the displacement amplitude a_x and therefore also the Allan deviation for $\tau \ll \tau_c/\chi$ depend on the resonator's phase shift ϕ . Therefore, for the sake of simplicity and without loss of generality, the Allan deviation will only be analyzed at fixed displacement amplitude hereafter.

The analysis also shows that the smallest possible value of χ is 1 and therefore the Allan deviation is larger than σ_{y0} at $\tau \gg \tau_c$ if $\chi > 1$; see Eq. (22). However, ϕ can be chosen such that $\chi = 1$ for any displacement amplitude [see Fig. 4(a)]. From Eq. (23), we can obtain an analytic expression for this optimal phase point ϕ^* :

$$\phi^* = \arctan\left(\frac{\sqrt{3}}{4\hat{a}^2}\right). \quad (25)$$

If this phase shift is fixed by the feedback, the Allan deviation will be the same as for a linear resonator oscillating at resonance at the corresponding a_x for any integration time. This condition has been previously referred to as

the amplitude detachment point [24]. Several works have pointed out the possibility of tuning the phase of a Duffing resonator in order to reduce the phase noise [21,24–26]. These efforts discussed several cases that are particularly interesting for improving the stability of time references. Nevertheless, fixing this phase condition entails difficulties that might prevent its practicality in sensing. First, as visualized in Fig. 4(a), χ becomes extremely sensitive to ϕ in the vicinity of $\phi = \phi^*$ as \hat{a} becomes greater than 1. Second, for a given displacement setpoint a_x , a higher force is needed at phase $\phi = \phi^*$ than at $\phi = -\pi/2$. By using Eqs. (10) and (25), it is deduced that the force needed to drive the resonator at ϕ^* is higher than that needed at $\phi = -\pi/2$ by a factor that grows with a_x^2 ; see Fig. 4(c). The higher force amplitude can introduce higher noise, which might prevent reaching the thermomechanical limit. For these practical reasons, the focus of the present work is on Duffing resonators operated at resonance, i.e., $\phi = -\pi/2$. This condition minimizes the influence of small deviations of ϕ on sensor resolution, and maximizes the conversion of force to displacement.

Under the oscillation condition $\phi = -\pi/2$ and assuming a displacement amplitude well above the critical amplitude ($\hat{a} \gg \sqrt[4]{3}/2$), then $\chi \approx 4\hat{a}^2/\sqrt{3}$. A graphic representation of Eqs. (20)–(22) under these assumptions is shown in Fig. 3(b). As seen, the Allan deviation reaches a minimum in the range $\tau \ll \tau_c$. This minimum value can be found by evaluating $\sigma_{y0}(\tau)$ at the boundary between the short and intermediate integration times, i.e., $\tau = \tau_c/\chi$:

$$\sigma_{y|\min}(\tau \ll \tau_c) = \frac{\sqrt{3}}{2} \sqrt{\frac{k_B T \gamma}{Q k_1}}. \quad (26)$$

It is worth pointing out that the integration time at which this minimum Allan deviation is reached (τ_c/χ) is inversely proportional to the displacement amplitude at which the resonator is driven. On the contrary, the value of $\sigma_{y|\min}(\tau \ll \tau_c)$ is a characteristic of the resonator, and does not depend on the oscillation amplitude set by the closed-loop controller. As a result, the model shows that the frequency resolution of a Duffing resonator presents a lower boundary at short gate times ($\tau \ll \tau_c$) given by the Duffing coefficient, the linear stiffness, and the quality factor. Importantly, higher quality factors lead to resonators with better (lower) resolution limits at this τ regime, because at constant k_1 , T , and γ , the value of the minimum Allan deviation for any a_x is proportional to $Q^{-1/2}$. This conclusion extends that from previous works [7,8], which were based on the assumption that a minimum Allan deviation curve was reached at a certain displacement amplitude, with that curve maintaining the $\sigma_y \propto \tau^{-1/2}$ form of linear resonators. In contrast, the analysis provided here shows that the amplitude-phase noise conversion, described by Eq. (15), depends not only on the driving amplitude but also on the frequency of the amplitude and phase noise, defined as

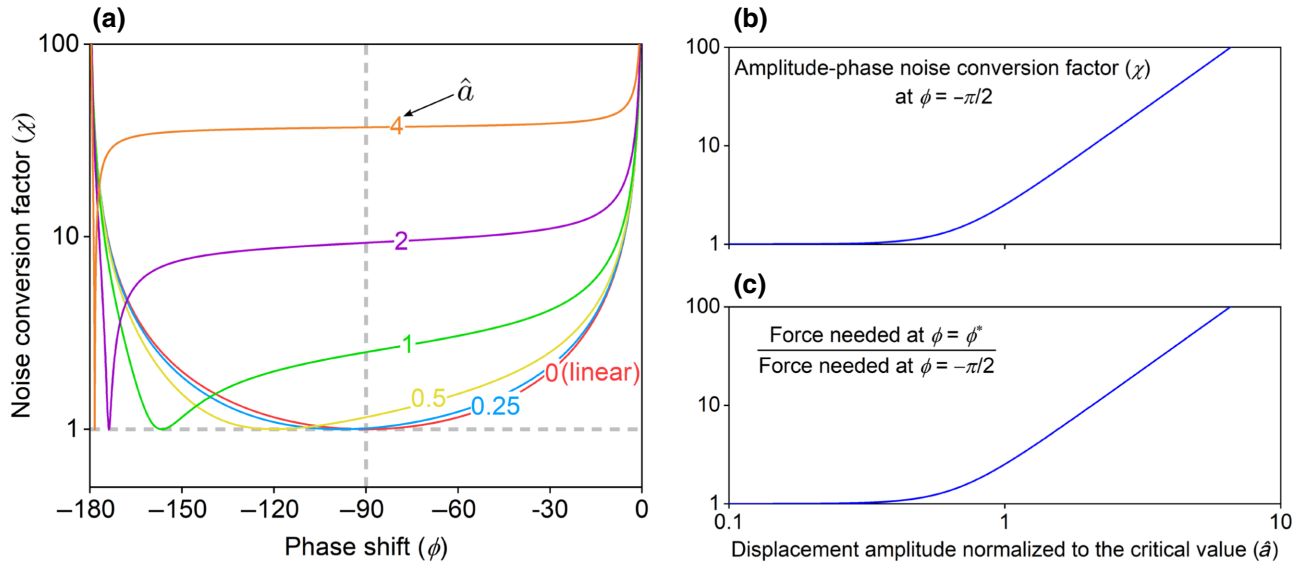


FIG. 4. (a) Factor χ accounting for the excess Allan deviation at $\tau \gg \tau_c$ due to the amplitude-phase noise conversion, with the phase shift ϕ in the horizontal axis. Each curve, obtained from Eq. (23), represents a different value of the displacement amplitude normalized to the critical value (\hat{a}), indicated by labels. (b) Factor χ for a resonator operated at $\phi = -\pi/2$, with \hat{a} in the horizontal axis. For low values of \hat{a} , a Duffing resonator behaves as a linear resonator, with $\chi \approx 1$. (c) Force needed to set a given value of \hat{a} with $\phi = \phi^*$, divided by the force needed to set the same value of \hat{a} with $\phi = -\pi/2$. This curve is obtained from Eq. (10).

an offset from the carrier frequency. As a consequence, the excess Allan deviation due to the amplitude-phase noise conversion depends on the integration time as well, yielding a minimum Allan deviation given by Eq. (26) for $\tau \ll \tau_c$. The model also shows that, for long averaging times $\tau \gg \tau_c$, the minimum Allan deviation indeed presents a $\tau^{-1/2}$ dependence that is reached at a displacement amplitude close to the critical value, in accordance with previous works [7,8]. Specifically, we find that Eq. (22) is minimized for $\hat{a} = \sqrt[4]{3}/2 \approx 0.66$, which results in a minimum Allan deviation

$$\sigma_{y|\min}(\tau \gg \tau_c) = \sqrt{\frac{3k_B T \gamma}{k_1 \omega_0 \tau}}. \quad (27)$$

To compare the theoretical model to the experimental results in Fig. 2(e), the Allan deviation limit calculated with Eq. (26) is plotted as a horizontal dashed line. The experimental data for high actuation forces are in qualitative agreement with the model at $\tau \ll \tau_c$, with a diminishing Allan deviation at short integration times and an increasing Allan deviation at higher values of τ . In between these regions a minimum value is found that does not depend on the driving force and shows good agreement with the value calculated with Eq. (26). For integration times longer than τ_c , the $\tau^{-1/2}$ dependence is seen, consistent with Eq. (27).

IV. SIMULATIONS

A Duffing resonator embedded in a direct feedback oscillator (DFO) is simulated in MATLAB[®] to validate the analytical model. The full nonlinear dynamics of the resonator, as described by Eq. (4), is used in the simulations, with the details given in Appendix A. Figure 5 shows the simulation results for different oscillation amplitudes and $\phi = -\pi/2$ for $Q = 10^3$ in Figs. 5(a) and 5(c) and $Q = 10^4$ in Figs. 5(b) and 5(d). The other resonator parameters can be found in the figure caption. The results show good qualitative agreement with the model prediction for the minimum Allan deviation limits. The minimum Allan deviation for $\tau \ll \tau_c$ is confirmed as being independent of τ , but dependent on the quality factor. In Figs. 5(c) and 5(d), a color map is shown to visualize the locus of the optimal displacement amplitude that minimizes the Allan deviation for each τ , which is also in good agreement with the model. As seen, the optimal displacement amplitude is constant for $\tau \gg \tau_c$ but dependent on τ for $\tau \ll \tau_c$. As expected, the simulation results show that the model is not accurate in the vicinity of $\tau = \tau_c$. There, the Allan deviation slightly surpasses the limits defined in both regimes and the optimal displacement amplitude smoothly transitions between both regimes' predictions.

V. DISCUSSION

The obtained results provide new insights into the ultimate limits and optimum design of closed-loop resonant

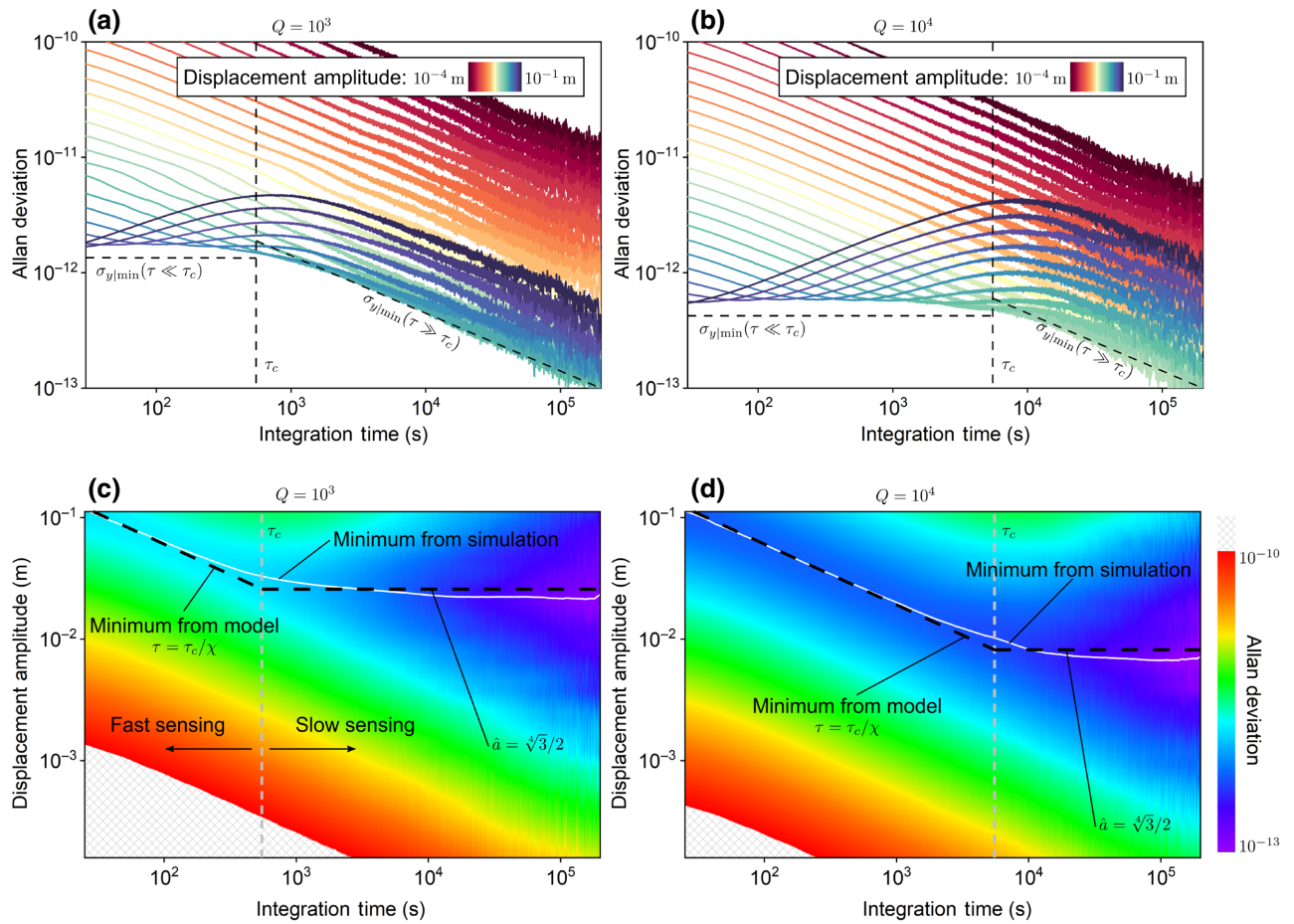


FIG. 5. Simulated Allan deviation for a Duffing resonator embedded in a direct feedback oscillator. The resonator parameters are $f_0 = 1$ Hz, $k_1 = 1$ N m $^{-1}$, $\gamma = 1$ m $^{-2}$. The temperature is assumed to be 300 K. (a),(b) Each curve represents the Allan deviation as a function of the integration time for a different displacement amplitude in the range from 10^{-4} to 10^{-1} m for $\phi = -\pi/2$ and a quality factor of (a) 10^3 and (b) 10^4 . The minimum Allan deviation found by the model is indicated for each case by black dashed lines. (c),(d) Color maps based on the same simulations. The Allan deviation is represented as a function of the displacement amplitude and integration time for a quality factor of (c) 10^3 and (d) 10^4 . The white solid lines (smoothed) mark the displacement amplitude that minimizes the Allan deviation for each integration time simulated. The black dashed lines indicate the optimal displacement predicted by the model.

sensors that operate at their resonance frequency ($\phi = -\pi/2$). In particular, in the fast-sensing regime, where the acquisition rate $f_s = 1/\tau$ of the sensor needs to exceed $1/\tau_c$, sensor optimization needs to proceed along different lines, and operation in the nonlinear regime becomes favorable. The oscillation amplitude that minimizes the Allan deviation in this regime for a given f_s can be found by setting the acquisition rate to $f_s = \chi/\tau_c$. Using Eq. (23) for displacement amplitudes well above the critical amplitude ($\hat{a} \gg \sqrt[4]{3}/2$) and Eq. (24), the optimal displacement normalized to the critical amplitude is found as

$$\hat{a}_{\text{fast}} = \sqrt{\frac{3Qf_s}{2\omega_0}} \quad (28)$$

with a non-normalized value of

$$a_{x|\text{fast}} = \hat{a}_{\text{fast}} a_{\text{crit}} = \frac{2}{\sqrt[4]{3}} \sqrt{\frac{f_s}{\omega_0 \gamma}}. \quad (29)$$

For this situation, the ultimate frequency resolution is given by Eq. (26) and can therefore be minimized by increasing the quality factor and the linear stiffness, and decreasing the cubic stiffness. Decreasing the acquisition rate does not further improve the minimum frequency resolution, unless it is increased sufficiently, where, for $f_s = 1/\tau_c$, the slow-sensing regime is reached.

In the slow-sensing regime, the displacement amplitude that yields the minimum Allan deviation can be obtained

by minimizing Eq. (22), giving a normalized value of

$$\hat{a}_{\text{slow}} = \frac{\sqrt[4]{3}}{2} \quad (30)$$

and a non-normalized value of

$$a_{x|\text{slow}} = \hat{a}_{\text{slow}} a_{\text{crit}} = \sqrt{\frac{2}{3Q\gamma}}. \quad (31)$$

In this case, the ultimate frequency resolution is described by Eq. (27), and can therefore be minimized by increasing the resonance frequency and the linear stiffness, and decreasing the cubic stiffness. Noticeably, increasing the quality factor does not further improve the ultimate frequency resolution, but lowering the acquisition rate, i.e., increasing the integration time, does help.

Let us now reflect on the underlying mechanisms behind our findings. In the linear regime, increasing the oscillation amplitude or integration time increases the signal energy with respect to the noise energy, which results in a decrease of the Allan deviation as expressed by Eq. (3). When entering the nonlinear regime, via the Duffing curve, the resonance frequency becomes amplitude dependent and amplitude noise tends to be converted to frequency noise. This effect increases the Allan deviation by a factor χ with respect to the linear situation for long integration times, according to Eq. (22). However, for short integration times, the situation improves, because the resonator itself acts as a low-pass filter: it takes a settling time Q/f_0 before a thermal fluctuation in the force amplitude appears as a fluctuation in the displacement amplitude to be converted to a fluctuation in frequency. Thanks to this effect, which starts to become prominent for $\tau < \tau_c$, the Allan deviation reduces when decreasing τ , by a factor of approximately τ/τ_c . For very small values $\tau \ll \tau_c/\chi$, all effects of amplitude-to-frequency conversion are suppressed by this filtering effect to a level below the Allan deviation caused by thermal fluctuations in the force phase, and one is left with the same Allan deviation as that of a linear resonator, even though the resonator is driven in the nonlinear regime. Thus, one might say that, at short τ , the resonator itself filters out all the additional frequency fluctuations due to amplitude-to-frequency conversion in the nonlinear regime. Interestingly, the fact that the minimum Allan deviation for $\tau < \tau_c$ occurs at $\tau = \tau_c/\chi$, with $\chi = 4/\sqrt{3}a_x^2$ at the standard oscillation condition ($\phi = -\pi/2$), combined with the fact that the Allan deviation in the linear regime scales with $1/(a_x\sqrt{\tau})$ [see Eq. (3)], results in a minimum Allan deviation for short integration times that is independent of the oscillation amplitude. The integration time at which this minimum value is obtained can then be tuned via the oscillation amplitude a_x .

Let us now reflect on the underlying mechanisms behind our findings. We have identified two main time constants

of importance. First, we have the constant τ_c , which is very close to the characteristic time the linear resonator needs to reach steady state, i.e., Q/f_0 . Second, we have τ_c/χ , which characterizes the effect of increasing the displacement amplitude a_x . This time constant results from a trade-off between a relative reduction of the input phase noise when increasing a_x and the enhancement of phase noise by the amplitude-phase noise conversion due to the nonlinear stiffness term $(3/8)\gamma a_x^2$ of Eq. (7). The combination of both contributions has a minimum at $\tau = \tau_c/\chi$ that provides an optimal operation point for Duffing resonators at the fast-sensing regime.

If a high acquisition frequency is not required, the oscillation amplitude a_x can be reduced, increasing τ_c/χ at constant minimum Allan deviation. This can continue until $a_x = a_{x|\text{slow}}$ is reached, which presents the optimal situation for the slow-sensing regime and results in $\chi = \sqrt{2}$. The remarkable fact is that if the acquisition frequency is decreased further ($f_s < 1/\tau_c$) at constant displacement amplitude a_x , it no longer results in an increase in the Allan deviation. Instead, the Allan deviation reduces proportionally to $f_s^{1/2}$ like in the linear regime. This behavior in the slow-sensing regime might be explained by the fact that the integration times are significantly longer than the characteristic time constant of the resonator, Q/f_0 . All force fluctuations at shorter time scales are averaged out, with the resonator acting as a low-pass filter for the amplitude and phase perturbations.

For completeness, it must be noted that the closed-loop tracking system for the resonance frequency behaves as a low-pass filter for the phase noise, and can be described by additional time constants [17]. These are set by the proportional-integral controller in a PLL, or by the amplifier bandwidth in a DFO. Nevertheless, a prerequisite for a closed-loop resonant sensor is that the resonance frequency tracking must be faster than the sensor acquisition rate, i.e., $f_s \ll 1/\tau_{\text{cl}}$, where τ_{cl} is the lowest time constant of the closed-loop phase-space transfer function of the system. Therefore, for a properly designed closed-loop system, the controller dynamics can be disregarded when analyzing the resolution limits [7].

The simulation results show, in accordance with the analytical model, that the minimum Allan deviation is reached for a different curve of Figs. 5(a) and 5(b), i.e., different amplitude, at each integration time in the fast-sensing regime. On the contrary, for slow sensing, the minimum is reached for each integration time by the same curve, i.e., same amplitude. Plotting the locus of these minima results in the asymptotic behavior shown in Fig. 1(c). It follows that increasing the quality factor of a Duffing resonator has two beneficial effects. First, the resonator will ultimately be more sensitive in the fast-sensing regime. Second, the integration time defining the fast-sensing regime will become longer, enabling better Allan deviations over a larger range of τ . The ultimate frequency resolution in the slow-sensing

regime will be unaltered by the change in the quality factor.

Another important consideration is that the minimum Allan deviation limit found for fast sensing, $\sigma_{y|\min}(\tau \ll \tau_c)$, can be reached for any integration time $\tau \ll \tau_c$ (acquisition rate $f_s \gg 1/\tau_c$) in a Duffing resonator, by tuning the displacement amplitude according to Eq. (29). This means that this frequency resolution can be achieved for arbitrarily high sensing speeds, assuming that the controller can be made fast enough. The higher the required speed (shorter integration time), the higher the displacement amplitude needed. In real resonators, nonlinear behaviors beyond the Duffing model, such as nonlinear damping, will emerge for high enough displacements, which will presumably limit the sensing speed at which $\sigma_{y|\min}(\tau \ll \tau_c)$ can be attained.

Finally, mass sensing is an application of utmost importance for the mechanical resonator community. In this context, the mass resolution δ_m can be related to the frequency resolution (Allan deviation) through the expression $\delta_m(\tau) = 2m\sigma_y(\tau)$ [1]. Then, the minimum mass resolution for fast sensing can be obtained by using Eq. (26):

$$\delta_{m|\min}(\tau \ll \tau_c) = \frac{\sqrt[4]{3}}{\omega_0} \sqrt{\frac{k_B T m \gamma}{Q}}. \quad (32)$$

Likewise, for slow sensing, Eq. (27) gives

$$\delta_{m|\min}(\tau \gg \tau_c) = \sqrt{\frac{12k_B T m \gamma}{\omega_0^3 \tau}}. \quad (33)$$

These two expressions can be applied to specific types of vibration modes for which analytical expressions for γ can be derived in order to optimize designs for best mass resolution. In Appendix E, the specific case of doubly clamped beams is analyzed.

VI. CONCLUSION

Previous knowledge suggested that the best frequency resolution of a resonant sensor with Duffing nonlinearity operated at resonance is that attained when the oscillation amplitude is set at the onset of nonlinearity. We present evidence that operation at higher amplitudes leads to lower frequency resolution at high acquisition rates $f_s \gg 1/\tau_c$. Whereas the resolution of resonant sensors in the low-speed regime ($f_s \ll \tau_c$) can be theoretically improved indefinitely by decreasing the acquisition rate, the resolution in the high-speed regime ($f_s \gg \tau_c$) is fundamentally limited by a lower boundary independent of the acquisition rate. In addition, we find that the ultimate frequency resolution in the fast-sensing regime improves when maximizing the quality factor of the resonator.

The reported experimental results, analytical model, and numerical analysis provide a roadmap for device optimization and concept development to drive down the

performance limits of resonant sensors. This understanding is expected to impact sensing applications requiring extreme resolution and high measurement rates simultaneously, such as the mass characterization of biomolecules with high throughput.

ACKNOWLEDGMENTS

This research work has received funding from the European Union's Horizon 2020 research and innovation programme under the Marie Skłodowska-Curie Grant Agreement No. 707404 and under Grant Agreement No. 881603 (Graphene Flagship). F.A. acknowledges financial support from European Research Council (ERC) Starting Grant No. 802093. M.X. and R.N. acknowledge financial support from Dutch Research Council (NWO) Startup research programme, under grant No. 740.018.020. The opinions expressed in this document reflect only the authors' views. The European Commission is not responsible for any use that may be made of the information it contains.

APPENDIX A: MATERIALS AND METHODS

1. Device fabrication

For the fabrication of 2×2 mm² nanomechanical membranes, a 92-nm-thick Si₃N₄ film with 1.1-GPa tensile stress is deposited by low-pressure chemical vapor deposition on a silicon wafer. After this, the wafer is diced into 10×10 mm² chips. On one of the chips, a square array of circular holes with radius 0.75 μm and center-to-center distance 3.5 μm in both x and y directions is created on the Si₃N₄ film. A single hole with a radius of 10 μm is created in the center of the pattern as a position indicator. The holes are defined by using electron-beam lithography on a positive tone photoresist (AR-P 6200), and subsequent inductively coupled plasma (ICP) reactive ion etching based on CHF₃. The resist is then removed by dimethylformamide; next the organic residues are cleaned with piranha solution (sulfuric acid to hydrogen peroxide 3:1; CAUTION: highly corrosive and dangerous to skin), and the remaining surface oxides are removed with hydrofluoric acid solution. The holes are then used to define and release the membrane area by isotropically etching the Si substrate using ICP etching based on SF₆ at -120 °C.

2. Experimental setup

The silicon chip containing the membrane is placed on a piezoactuator for the experiments. All the measurements are performed inside a vacuum chamber at a pressure of 2 mPa. Thanks to a glass window on the vacuum chamber, the vibrations are recorded by a Doppler laser vibrometer (Polytec MSA400). The actuation signal is provided to the piezoactuator by a digital lock-in (Zurich Instruments HF2LI). The same instrument is used to record the displacement signal from the vibrometer. The

PSD of the displacement is first recorded with no signal applied to the piezoactuator [Fig. 2(c)]. Then, frequency sweeps around the resonance are performed for various voltage amplitudes applied to the piezoactuator [Fig. 2(d)]. The resonator's transfer function, obtained through fitting the data from these experiments, allows us to obtain the conversion factor from voltage to force associated with the piezo-actuator-chip assembly. For the Allan deviation experiments, the digital lock-in is configured in PLL mode, with a phase detector filter of order 8 and bandwidth 18 kHz. The proportional-integral controller is set with a proportional constant of 1.8×10^3 Hz and an integral constant of 5.4×10^3 Hz², ensuring enough PLL bandwidth to characterize integration times longer than 100 μ s. The target phase is set to the phase shift featured by the resonator at the frequency of maximum amplitude when actuated in the linear range, which corresponds to the theoretical point $\phi = -\pi/2$. Under these conditions, data series of the resonator phase and the drive frequency are recorded for 5 min with an acquisition rate of 7.2 kHz, while applying the force amplitudes shown in Fig. 2(d). White noise with a bandwidth of 9 MHz, provided by a waveform generator (Agilent 33220A), is introduced in the digital lock-in and superimposed to the actuation signal. For each force amplitude, the dimensionless Allan deviation is calculated from the drive frequency data in MATLAB.

3. Simulations

A DFO is simulated in MATLAB/SIMULINK including the full nonlinear differential equation of a Duffing resonator. The DFO is formed by the resonator and an amplifier-phase shifter chain, which generates a force proportional to the resonator's displacement. The amplifier gain is set such that the closed-loop gain of the system is slightly above 1. From Eq. (10), this is achieved by an amplifier gain of $-k_1/(Q \sin \phi)$. For stable oscillations, a saturation element is included in the feedback to set the oscillation amplitude to an arbitrary value a_x . The phase shifter is fixed to $\pi/2$, which ensures that the Barkhausen criterion is met for a resonator phase $\phi = -\pi/2$, and the oscillation frequency is ω_p . The amplifier, phase shifter, and saturation are modeled as noiseless elements with infinite bandwidth. To include the thermomechanical noise affecting the resonator, a random force with white PSD in accordance to Eq. (2) is superimposed to the force applied by the feedback to the resonator. The phase of the resonator displacement is calculated through a phase detector scheme and used to obtain the dimensionless Allan deviation following expression A.23 in Ref. [6]. The simulated time is 2×10^5 s and the time step is fixed to the inverse of the linear resonance frequency divided by 100. The default fixed-step solver of SIMULINK is used.

APPENDIX B: LINEARIZED MODEL OF THE AMPLITUDE-PHASE SPACE OF A DUFFING RESONATOR UNDER CLOSED-LOOP OPERATION

System (6)–(8) can be linearized around a fixed point defined by a pair of values $a_x = a_{x0}$ and $\phi = \phi_0$, which unambiguously define $a_g = a_{g0}$ and $\psi = \psi_0$ according to Eqs. (10) and (11). To express the linearized system in the state-space representation, the states are defined as the perturbations of the amplitude and phase of the resonator's displacement, Δa_x and $\Delta \phi_x$, that coincide with the system outputs. The system inputs are defined as the perturbations of the amplitude and phase of the force acting on the resonator, Δa_g and $\Delta \phi_g$, respectively. This results in a system defined by matrices D and E :

$$\begin{bmatrix} \Delta \dot{a}_x \\ \Delta \dot{\phi}_x \end{bmatrix} = \begin{bmatrix} D_{11} & D_{12} \\ D_{21} & D_{22} \end{bmatrix} \begin{bmatrix} \Delta a_x \\ \Delta \phi_x \end{bmatrix} + \begin{bmatrix} E_{11} & E_{12} \\ E_{21} & E_{22} \end{bmatrix} \begin{bmatrix} \Delta a_g \\ \Delta \phi_g \end{bmatrix} \quad (\text{B1})$$

with the elements of the matrices given by

$$D_{11} = \left. \frac{\partial \eta_a}{\partial a_x} \right|_{a_{x0}, \phi_0, a_{g0}, \psi_0} = -\Gamma, \quad (\text{B2})$$

$$D_{12} = \left. \frac{\partial \eta_a}{\partial \phi_x} \right|_{a_{x0}, \phi_0, a_{g0}, \psi_0} = \frac{\Gamma a_{x0}}{\tan \phi_0}, \quad (\text{B3})$$

$$D_{21} = \left. \frac{\partial \eta_\phi}{\partial a_x} \right|_{a_{x0}, \phi_0, a_{g0}, \psi_0} = \frac{3}{4} \gamma a_{x0} - \frac{\Gamma}{a_{x0} \tan \phi_0}, \quad (\text{B4})$$

$$D_{22} = \left. \frac{\partial \eta_\phi}{\partial \phi_x} \right|_{a_{x0}, \phi_0, a_{g0}, \psi_0} = -\Gamma, \quad (\text{B5})$$

$$E_{11} = \left. \frac{\partial \eta_a}{\partial a_g} \right|_{a_{x0}, \phi_0, a_{g0}, \psi_0} = -\frac{\sin \phi_0}{2}, \quad (\text{B6})$$

$$E_{12} = \left. \frac{\partial \eta_a}{\partial \phi_g} \right|_{a_{x0}, \phi_0, a_{g0}, \psi_0} = -\frac{\Gamma a_{x0}}{\tan \phi_0}, \quad (\text{B7})$$

$$E_{21} = \left. \frac{\partial \eta_\phi}{\partial a_g} \right|_{a_{x0}, \phi_0, a_{g0}, \psi_0} = -\frac{\cos \phi_0}{2a_{x0}}, \quad (\text{B8})$$

$$E_{22} = \left. \frac{\partial \eta_\phi}{\partial \phi_g} \right|_{a_{x0}, \phi_0, a_{g0}, \psi_0} = \Gamma. \quad (\text{B9})$$

This system can be represented in the Laplace domain to obtain

$$\begin{bmatrix} A_x(s) \\ \Phi_x(s) \end{bmatrix} = \begin{bmatrix} H_{11}(s) & H_{12}(s) \\ H_{21}(s) & H_{22}(s) \end{bmatrix} \begin{bmatrix} A_g(s) \\ \Phi_g(s) \end{bmatrix}, \quad (\text{B10})$$

where $A_x(s)$, $\Phi_x(s)$, $A_g(s)$, and $\Phi_g(s)$ are the Laplace transforms of Δa_x , $\Delta \phi_x$, Δa_g , and $\Delta \phi_g$, respectively. The transfer function matrix can be found by setting

$H(s) = (s\mathbb{I} - D)^{-1}E$, where \mathbb{I} is the identity matrix of size 2 [27]. This yields

$$H_{11}(s) = \frac{s(\cos(2\phi_0) - 1) - 2\Gamma}{P \sin \phi_0}, \quad (\text{B11})$$

$$H_{12}(s) = -\frac{4s\Gamma a_{x0}}{P \tan \phi_0}, \quad (\text{B12})$$

$$H_{21}(s) = -\frac{4s \cos \phi_0 + 3\gamma a_{x0}^2 \sin \phi_0}{2Pa_{x0}}, \quad (\text{B13})$$

$$H_{22}(s) = \frac{\Gamma(4(s + \Gamma) - 3\gamma a_{x0}^2/\tan \phi_0 + 4\Gamma/\tan^2 \phi_0)}{P}, \quad (\text{B14})$$

with $P = 4(\Gamma + s)^2 + 4\Gamma^2/\tan^2 \phi_0 - 3\gamma a_{x0}^2/\tan \phi_0$.

As discussed in the main text, a closed-loop control is needed to keep the resonator at the fixed point. Its effect on the amplitude and phase perturbations is accounted for by a matrix $B(s)$ in the feedback path, as depicted in Fig. 3(a). For a PLL scheme as used in the experiments, the phase perturbations are fed back by the phase detector-controller chain [6]. For frequencies lower than the bandwidth of the PLL transfer function, the dynamic behavior of the feedback path can be neglected [7]. This implies that the phase perturbations are passed from the input to the output of the controller with a gain of 1, as long as the PLL is faster than the maximum sensing speed of interest. On the other hand, the feedback controller of a PLL rejects the amplitude perturbations as it only detects the phase of the output signal. This results in a feedback matrix

$$B(s) = \begin{bmatrix} 0 & 0 \\ 0 & 1 \end{bmatrix}. \quad (\text{B15})$$

Alternatively to the PLL scheme, DFOs also provide a means to keep a resonator oscillating at a desired fixed point [24]. This type of system results from using an amplifier and phase shifter to feedback the resonator's displacement into its force. The phase shift ϕ_0 can be controlled by offsetting the loop phase through the phase shifter. As in the PLL case, the feedback path of a DFO lets the phase perturbations pass with gain 1 for perturbation frequencies lower than the bandwidth of the amplifier. To control the amplitude of oscillation a_{x0} , either a nonlinear saturation block or an automatic gain control (AGC) can be placed in the feedback path. The B matrix of a DFO can be approximated by Eq. (B15) as long as the amplitude control method used does not let the amplitude perturbations pass. Therefore, an AGC must allow for slow variations of the amplitude to allow the startup of the oscillations, while stopping fast variations. That is, it must behave as a low-pass filter for the amplitude perturbations. For perturbations with frequencies higher than the bandwidth of the AGC, the feedback effectively stops the

amplitude perturbations, and Eq. (B15) can be regarded as valid. To summarize, the present analysis is also valid for a DFO as long as the relevant frequencies of the amplitude and phase noise are higher than the bandwidth of the AGC but lower than the bandwidth of the amplifier. In the context of sensing, this implies that the AGC must be slower than the maximum integration time (minimum sensing speed) of interest, while the amplifier must be faster than the minimum integration time (maximum sensing speed) of interest.

Given the $H(s)$ and $B(s)$ matrices, the closed-loop transfer function matrix $J(s)$ that governs the dynamics of the amplitude and phase perturbations can be obtained by using the feedback equation

$$J(s) = [I - H(s)B(s)]^{-1}H(s), \quad (\text{B16})$$

which results in

$$J_{11}(s) = -\frac{\sin \phi_0}{2(s + \Gamma)}, \quad (\text{B17})$$

$$J_{12}(s) = -\frac{\Gamma a_{x0}}{\tan \phi_0(s + \Gamma)}, \quad (\text{B18})$$

$$J_{21}(s) = -\frac{3\gamma a_{x0}^2 \sin \phi_0 + 4s \cos \phi_0}{8a_{x0}s(s + \Gamma)}, \quad (\text{B19})$$

$$J_{22}(s) = \frac{\Gamma(4s - 3\gamma a_{x0}^2/\tan \phi_0 + 4\Gamma(1 + 1/\tan^2 \phi_0))}{4s(s + \Gamma)}. \quad (\text{B20})$$

For simplicity, a_{x0} and ϕ_0 have been renamed as a_x and ϕ , respectively, in the main text as well as in the appendices hereafter, unless noted otherwise.

APPENDIX C: BIAS OF THE ESTIMATOR FOR THE RESONANCE FREQUENCY UNDER CLOSED-LOOP OPERATION

The estimator defined by Eq. (12) is subjected to the noise present in the drive frequency, resulting from the amplitude and phase noise affecting the resonator. This can be accounted for by substituting $\omega = \omega_0(1 + (3/8)\gamma a_x^2 + \Gamma/\tan \phi)$ and letting a_x and ϕ be random variables:

$$\bar{\omega}_0 = \omega_0 \frac{1 + 3\gamma a_x^2/8 + \Gamma/\tan \phi}{1 + 3\gamma a_{x0}^2/8 + \Gamma/\tan \phi}. \quad (\text{C1})$$

For clarity, subindex 0 has been introduced to denote the fixed points, while a_x and ϕ represent the random amplitude and phase of the resonator. The statistical expectation, denoted $\mathbb{E}(\cdot)$, of the estimator is then

$$\mathbb{E}(\bar{\omega}_0) = \omega_0 \frac{1 + 3\gamma \mathbb{E}(a_x^2)/8 + \Gamma \mathbb{E}(1/\tan \phi)}{1 + 3\gamma a_{x0}^2/8 + \Gamma/\tan \phi}. \quad (\text{C2})$$

The displacement amplitude a_x follows a normal distribution with $\mathbb{E}(a_x) = a_{x0}$ and variance $k_B T/k_1$ [22]. It follows

that $\mathbb{E}(a_x^2) = a_{x0}^2 + k_B T/k_1$. For simplicity, we analyze the practical interesting case of $\phi_0 = -\pi/2$. With that choice, ϕ follows a normal distribution with $\mathbb{E}(\phi) = -\pi/2$, and the asymmetric nature of the \tan^{-1} function with respect to $-\pi/2$ results in $\mathbb{E}(\tan^{-1}(\phi)) = 0$. Substituting into Eq. (C2) results in

$$\mathbb{E}(\bar{\omega}_0) = \omega_0 \left(1 + \frac{k_B T}{k_1(8/(3\gamma) + a_{x0}^2)} \right). \quad (\text{C3})$$

The bias of the estimator normalized to the resonance frequency can be calculated as

$$\mathbb{B}(\bar{\omega}_0) = \frac{\mathbb{E}(\bar{\omega}_0) - \omega_0}{\omega_0} = \frac{k_B T}{k_1(8/(3\gamma) + a_{x0}^2)}. \quad (\text{C4})$$

For the resonator used in our experiments at room temperature, this bias is 5 orders of magnitude below the minimum Allan deviation predicted by Eq. (26). The resonator would need a quality factor of the order of 1×10^{15} for this bias to be of the same order of magnitude as the minimum Allan deviation predicted by our model.

APPENDIX D: PHASE NOISE AND ALLAN DEVIATION OF A DUFFING RESONATOR UNDER CLOSED-LOOP OPERATION

The PSD of the displacement phase noise for a closed-loop Duffing resonator dominated by thermomechanical noise is obtained from Eq. (19):

$$S_{\phi x}(\omega) = |J_{21}(i\hat{\omega})|^2 S_{a|\text{thm}} + |J_{22}(i\hat{\omega})|^2 S_{\phi|\text{thm}}. \quad (\text{D1})$$

The result can be expressed as

$$S_{\phi x}(f) = \frac{G(f^2 + \chi^2 f_c^2)}{f^2(f^2 + f_c^2)}, \quad (\text{D2})$$

where f represents the frequency offset from the carrier frequency, and the constants are given by

$$G = \frac{k_B T}{2\pi^2 m Q \omega_0 a_x^2}, \quad (\text{D3})$$

$$f_c = \frac{f_0}{2Q}, \quad (\text{D4})$$

$$\chi = \frac{1}{2} \sqrt{9\gamma^2 Q^2 a_x^4 + 4/\sin^2 \phi - 12\gamma Q a_x^2 / \tan \phi}. \quad (\text{D5})$$

Factor χ accounts for the amplitude-phase noise conversion arising from the Duffing characteristic or from operating the resonator at $\phi \neq -\pi/2$. A linear resonator ($\gamma = 0$) operated at $\phi = -\pi/2$ gives $\chi = 1$, which results in $S_{\phi x}(f) = G/f^2$. Note that χ is real and larger than 1 for $\phi \in (-\pi, 0)$.

Assuming strong noise conversion ($\chi \gg 1$), three frequency ranges can be defined in which the derived phase noise is approximated by the asymptotes of Eq. (D2):

$$S_{\phi x}(f \ll f_c) = G\chi^2 \frac{1}{f^2}, \quad (\text{D6})$$

$$S_{\phi x}(f_c \ll f \ll \chi f_c) = G\chi^2 f_c^2 \frac{1}{f^4}, \quad (\text{D7})$$

$$S_{\phi x}(f \gg \chi f_c) = G \frac{1}{f^2}. \quad (\text{D8})$$

Note that, for $f \gg \chi f_c$, there is no effect of the amplitude-phase noise conversion, and the phase noise is the same as for a linear resonator operated at resonance.

The Allan deviation σ_y can be obtained from the PSD of the displacement phase noise through the integral expression [3]

$$\sigma_y^2(\tau) = 2 \int_0^{+\infty} S_{\phi x}(f) \frac{\sin^4(\pi f \tau)}{(\pi f \tau)^2} df, \quad (\text{D9})$$

where τ is the integration time. Simplified expressions for its evaluation at each of the frequency ranges defined above can be found in Ref. [3]. The phase noise at each frequency range can be converted to Allan deviation for a corresponding integration time range. The phase noise for high frequencies ($f \gg \chi f_c$) determines the Allan deviation for short integration times below a certain value of τ_c/χ . Therefore, by substituting Eq. (D8) into Eq. (D9), we obtain

$$\sigma_y(\tau \ll \tau_c/\chi) = \frac{1}{a_x} \sqrt{\frac{k_B T}{m Q \omega_0^3 \tau}} = \sigma_{y0}, \quad (\text{D10})$$

where σ_{y0} is the Allan deviation of a linear resonator operated at $\phi = -\pi/2$. Likewise, the phase noise for $f \ll f_c$ dominates the Allan deviation for integration times longer than τ_c . Therefore, by substituting Eq. (D6) into Eq. (D9), we obtain

$$\sigma_y(\tau \gg \tau_c) = \chi \sigma_{y0}. \quad (\text{D11})$$

From the phase noise at intermediate frequencies, the Allan deviation at intermediate integration times is obtained. Therefore, by substituting Eq. (D7) into Eq. (D9), we obtain

$$\sigma_y(\tau_c/\chi \ll \tau \ll \tau_c) = \frac{\pi}{\sqrt{3}} \frac{f_0 \tau}{Q} \chi \sigma_{y0}. \quad (\text{D12})$$

By setting $\sigma_y(\tau \gg \tau_c) = \sigma_y(\tau_c/\chi \ll \tau \ll \tau_c)$ and resolving for τ , we find that

$$\tau_c = \frac{\sqrt{3} Q}{\pi f_0}. \quad (\text{D13})$$

APPENDIX E: RESOLUTION LIMITS OF A DOUBLY CLAMPED BEAM

We can particularize the mass resolution limits found to the widely studied resonators based on doubly clamped beams. For a rectangular beam of length l , width w , thickness h , mass density ρ , and Young's modulus Y , we can express the Duffing coefficient associated with the fundamental mode as [28]

$$\gamma = \frac{2}{h^2}, \quad (\text{E1})$$

the linear stiffness as [14]

$$k_1 = \frac{16Ywh^3}{l^3}, \quad (\text{E2})$$

and the fundamental resonance frequency as [29]

$$\omega_0 = \frac{\lambda_0^2 h}{l^2} \sqrt{\frac{Y}{12\rho}} \quad (\text{E3})$$

with $\lambda_0 = 4.73$. By combining these expressions with Eq. (26), we obtain

$$\sigma_{y|\min}(\tau \ll \tau_c) = \frac{\sqrt[4]{3}}{\sqrt{32}} \sqrt{\frac{k_B T l^3}{Q Y h^5 w}}. \quad (\text{E4})$$

Doing the same with Eq. (27), we obtain

$$\sigma_{y|\min}(\tau \gg \tau_c) = \frac{1}{2\lambda_0} \sqrt[4]{\frac{27\rho}{Y^3}} \sqrt{\frac{k_B T l^5}{h^6 w \tau}}. \quad (\text{E5})$$

We can also calculate the minimum mass resolution at both regimes by setting $\delta_m = 2m\sigma_y$ with $m = k_1/\omega_0^2$:

$$\delta_{m|\min}(\tau \ll \tau_c) = \frac{192\sqrt[4]{3}\rho}{\sqrt{8}\lambda_0^4} \sqrt{\frac{k_B T l^5 w}{Q Y h^3}}, \quad (\text{E6})$$

$$\delta_{m|\min}(\tau \gg \tau_c) = \frac{192\sqrt[4]{27}}{\lambda_0^5} \sqrt[4]{\frac{\rho^5}{Y^3}} \frac{1}{h^2} \sqrt{\frac{k_B T l^7}{\tau}}. \quad (\text{E7})$$

These expressions establish the ultimate mass resolution of a doubly clamped beam due its geometrical nonlinearity, as a function of the material properties, dimensions, quality factor, and temperature.

-
- [1] K. Ekinici, Y. T. Yang, and M. Roukes, Ultimate limits to inertial mass sensing based upon nanoelectromechanical systems, *J. Appl. Phys.* **95**, 2682 (2004).
 [2] D. W. Allan, Statistics of atomic frequency standards, *Proc. IEEE* **54**, 221 (1966).

- [3] J. A. Barnes, A. R. Chi, L. S. Cutler, D. J. Healey, D. B. Leeson, T. E. McGunigal, J. A. Mullen, W. L. Smith, R. L. Sydnor, and R. F. Vessot, *et al.*, Characterization of frequency stability, *IEEE Trans. Instrum. Meas.* **IM-20**, 105 (1971).
 [4] A. Cleland and M. Roukes, Noise processes in nanomechanical resonators, *J. Appl. Phys.* **92**, 2758 (2002).
 [5] M. Sansa, E. Sage, E. C. Bullard, M. Gély, T. Alava, E. Colinet, A. K. Naik, L. G. Villanueva, L. Duraffourg, and M. L. Roukes, *et al.*, Frequency fluctuations in silicon nanoresonators, *Nat. Nanotechnol.* **11**, 552 (2016).
 [6] T. Manzanogue, P. G. Steeneken, F. Alijani, and M. K. Ghatkesar, Method to determine the closed-loop precision of resonant sensors from open-loop measurements, *IEEE Sens. J.* **20**, 14262 (2020).
 [7] A. Demir and M. S. Hanay, Fundamental sensitivity limitations of nanomechanical resonant sensors due to thermomechanical noise, *IEEE Sens. J.* **20**, 1947 (2019).
 [8] S. K. Roy, V. T. Sauer, J. N. Westwood-Bachman, A. Venkatasubramanian, and W. K. Hiebert, Improving mechanical sensor performance through larger damping, *Science* **360**, eaar5220 (2018).
 [9] S. Olcum, N. Cermak, S. C. Wasserman, K. S. Christine, H. Atsumi, K. R. Payer, W. Shen, J. Lee, A. M. Belcher, and S. N. Bhatia, *et al.*, Weighing nanoparticles in solution at the attogram scale, *Proc. Nat. Acad. Sci.* **111**, 1310 (2014).
 [10] J. Molina, J. E. Escobar, D. Ramos, E. Gil-Santos, J. J. Ruz, J. Tamayo, Á. San Paulo, and M. Calleja, High dynamic range nanowire resonators, *Nano Lett.* **21**, 6617 (2021).
 [11] T. Ando, T. Uchihashi, and T. Fukuma, High-speed atomic force microscopy for nano-visualization of dynamic biomolecular processes, *Prog. Surf. Sci.* **83**, 337 (2008).
 [12] A. K. Naik, M. Hanay, W. Hiebert, X. Feng, and M. L. Roukes, Towards single-molecule nanomechanical mass spectrometry, *Nat. Nanotechnol.* **4**, 445 (2009).
 [13] M. Febbo and J. Ji, On the critical forcing amplitude of forced nonlinear oscillators, *Open Eng.* **3**, 764 (2013).
 [14] B. Hauer, C. Doolin, K. Beach, and J. Davis, A general procedure for thermomechanical calibration of nano/micromechanical resonators, *Ann. Phys. (N. Y.)* **339**, 181 (2013).
 [15] F. Yang, F. Hellbach, F. Rochau, W. Belzig, E. M. Weig, G. Rastelli, and E. Scheer, Persistent Response in an Ultra-strongly Driven Mechanical Membrane Resonator, *Phys. Rev. Lett.* **127**, 014304 (2021).
 [16] A. Nayfeh and D. Mook, *Nonlinear Oscillations*, Wiley Classics Library (Wiley, Weinheim, Germany, 2008).
 [17] S. Olcum, N. Cermak, S. C. Wasserman, and S. R. Manalis, High-speed multiple-mode mass-sensing resolves dynamic nanoscale mass distributions, *Nat. Commun.* **6**, 1 (2015).
 [18] V. Denis, M. Jossic, C. Giraud-Audine, B. Chomette, A. Renault, and O. Thomas, Identification of nonlinear modes using phase-locked-loop experimental continuation and normal form, *Mech. Syst. Signal Process.* **106**, 430 (2018).
 [19] J. M. L. Miller, A. Ansari, D. B. Heinz, Y. Chen, I. B. Flader, D. D. Shin, L. G. Villanueva, and T. W. Kenny, Effective quality factor tuning mechanisms in micromechanical resonators, *Appl. Phys. Rev.* **5**, 041307 (2018).
 [20] H. B. Callen and T. A. Welton, Irreversibility and generalized noise, *Phys. Rev.* **83**, 34 (1951).

- [21] E. Kenig, M. Cross, L. Villanueva, R. Karabalin, M. Matheny, R. Lifshitz, and M. Roukes, Optimal operating points of oscillators using nonlinear resonators, *Phys. Rev. E* **86**, 056207 (2012).
- [22] M. Wang, R. Zhang, R. Ilic, Y. Liu, and V. A. Aksyuk, Fundamental limits and optimal estimation of the resonance frequency of a linear harmonic oscillator, *Commun. Phys.* **4**, 207 (2021).
- [23] E. Rubiola, *Phase Noise and Frequency Stability in Oscillators* (Cambridge University Press, Cambridge, UK, 2008).
- [24] L. Villanueva, E. Kenig, R. Karabalin, M. Matheny, R. Lifshitz, M. Cross, and M. Roukes, Surpassing Fundamental Limits of Oscillators Using Nonlinear Resonators, *Phys. Rev. Lett.* **110**, 177208 (2013).
- [25] R. M. Mestrom, R. H. Fey, and H. Nijmeijer, Phase feedback for nonlinear MEM resonators in oscillator circuits, *IEEE ASME Trans. Mechatron.* **14**, 423 (2009).
- [26] B. Yurke, D. Greywall, A. Pargellis, and P. Busch, Theory of amplifier-noise evasion in an oscillator employing a nonlinear resonator, *Phys. Rev. A* **51**, 4211 (1995).
- [27] B. Friedland, *Control System Design: An Introduction to State-Space Methods*, *Dover Books on Electrical Engineering* (Dover Publications, Mineola, NY, US, 2005).
- [28] H. Westra, *Nonlinear beam mechanics*, Ph.D. thesis, Delft University of Technology (2012).
- [29] R. Blevins, *Formulas for Natural Frequency and Mode Shape* (Krieger Publishing Company, New York, US, 2001).